

Full paper

Odometry Correction Using Visual Slip Angle Estimation for Planetary Exploration Rovers

Giulio Reina^{a,*}, Genya Ishigami^b, Keiji Nagatani^c and Kazuya Yoshida^c

^a Department of Engineering for Innovation, University of Salento, Via Arnesano, 73100 Lecce, Italy

^b Mechanical Engineering Department, Massachusetts Institute of Technology,
77 Massachusetts Avenue, Cambridge, MA 02139, USA

^c Department of Aerospace Engineering, Tohoku University, Aoba 6-6-01, Sendai 980-8579, Japan

Received 27 February 2009; accepted 10 June 2009

Abstract

This paper introduces a novel method for slip angle estimation based on visually observing the traces produced by the wheels of a robot on soft, deformable terrain. The proposed algorithm uses a robust Hough transform enhanced by fuzzy reasoning to estimate the angle of inclination of the wheel trace with respect to the vehicle reference frame. Any deviation of the wheel track from the planned path of the robot suggests occurrence of sideslip that can be detected and, more interestingly, measured. In turn, the knowledge of the slip angle allows encoder readings affected by wheel slip to be adjusted and the accuracy of the position estimation system to be improved, based on an integrated longitudinal and lateral wheel–terrain slip model. The description of the visual algorithm and the odometry correction method is presented, and a comprehensive set of experimental results is included to validate this approach.

© Koninklijke Brill NV, Leiden and The Robotics Society of Japan, 2010

Keywords

Planetary rovers, slip angle estimation, integrated longitudinal and lateral slip

1. Introduction

Wheel slippage is a critical issue for mobile robots driving across loose soil, such as dry sand and the like. It greatly affects the traction performance and energy consumption, and leads to gradual deviation of the vehicle from the intended path, possibly resulting in large drift and poor results of localization and control systems [1, 2]. For example, the use of the conventional dead-reckoning technique is largely compromised, since it is based on the assumption that wheel revolutions can be translated into correspondent linear displacements. Thus, if one wheel slips, then

* To whom correspondence should be addressed. E-mail: giulio.reina@unisalento.it

the associated encoder will register revolutions even though these revolutions do not correspond to a linear displacement of the wheel. Conversely, if one wheel skids, fewer encoder pulses will be counted.

Most of the research in the field of mobile robotics has been focusing on the study of slip along the longitudinal direction of motion. Longitudinal slip can be estimated through the use of encoders by comparing the speed of driven wheels to that of undriven wheels on asphalt [3]; however, this is not suitable for deformable surfaces and does not apply for all-wheel drive vehicles or those without redundant encoders. Reina *et al.* [4] proposed measures for longitudinal slip detection, based on comparing different onboard sensor modalities within a fuzzy logic inference engine. Ojeda *et al.* [5] presented a motor current-based slip estimator, while in Ref. [6] a Kalman filter-based approach combining encoders, inertial measurement units (IMUs) and GPS was discussed for detecting immobilization conditions of a mobile robot. However, in the presence of side forces, the robot moves at an angle (i.e., the slip angle) with respect to its longitudinal axis, resulting in lateral slip as well [7]. A large body of research work exists in the automotive community related to traction control, anti-lock braking systems and electronic stability programs. However, these works generally apply to asphalt roads and at significantly higher speeds than those typical for autonomous robots [8, 9]. In this area, Kalman filters have been widely applied to inertial and absolute measurements, such as GPS, to enhance dead reckoning and estimate lateral slip [10, 11]. However, GPS is not yet a feasible option for planetary applications.

This paper investigates the feasibility of a novel approach previously proposed by the authors [12] for slip angle estimation of mobile robots traveling on loose terrain, such as that planetary rovers are expected to encounter. This method is based on using a rearward-facing video camera to measure the pose of the trace that is produced by the wheels, and detect whether the robot follows the desired path or deviates from it because of slippage. Figure 1 shows a direct example that will help to clarify this method. For the extensive testing of the system during its development, we employed the rover El-Dorado, built at the Space Robotics Laboratory of Tohoku University. El-Dorado is an independently controlled four-wheel-drive/four-wheel-steer mobile robot, also featuring a rocker-type suspension system. Its operational speed ranges from 2 to 30 cm/s. In Fig. 1, the rear webcam is visible, mounted to a frame attached to vehicle's body. The robot is also equipped with wheel and steer encoders, and a fluxgate compass to measure the absolute vehicle heading. Figure 1a shows El-Dorado as driving up a sandy slope following a planned straight path without any significant sideslip. This is shown by two distinct traces parallel to the direction of motion and produced by the wheel pair of either side of the robot. However, if a transverse inclination of the terrain is also present, the consequent external side force acting on rover's body will result in a substantial lateral drift, as shown in Fig. 1b. The traces, left by the wheels of the same side of the robot, are no longer superimposed and, more importantly, their angle of inclination, with respect to a reference frame attached to the vehicle, differs from the case of absence of slip.

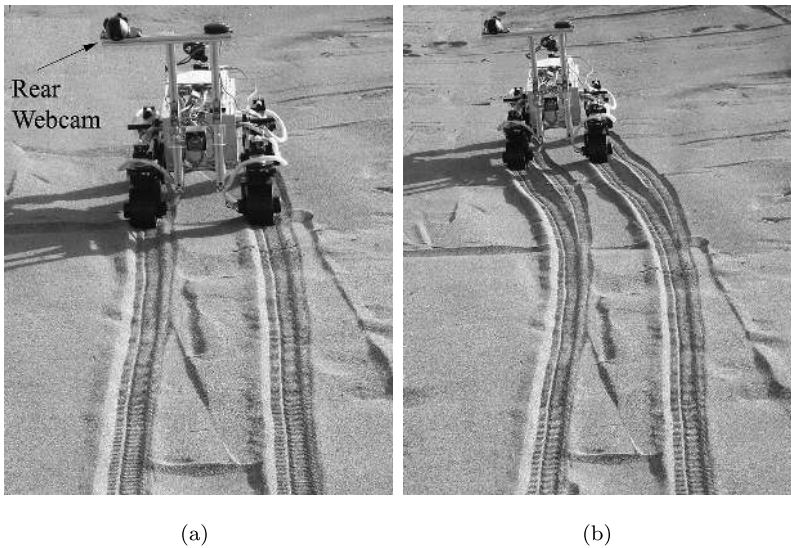


Figure 1. Sideslip estimation for a mobile robot by visual observation of the wheel traces with a rear webcam. (a) Wheel traces parallel to the direction of motion, no lateral slip. (b) Wheel traces inclined with respect to the intended direction of motion, significant lateral slip. Note the slight roll angle of the robot due to the transverse inclination of the terrain for case (b).

The proposed approach aims at estimating the slip angle of the robot by measuring the pose of one of the wheel traces, i.e., the rear left wheel, in conjunction with the knowledge of the rate of turn provided by an onboard sensor. In our terrestrial implementation and proof of concept, we employed a compass. However, for planetary applications a more appropriate sensor will be required, such as an IMU. Since our approach is based on Hough transform supported by Fuzzy logic to provide robust and accurate tracking of the wheel Trace, we call it ‘FTrace’.

In order to allow useful dead-reckoning even on high-slippage terrain, we present a method for slippage compensated odometry, called ‘sComp’. The system is based on an integrated longitudinal and lateral friction model, derived from a semiempirical approach. First, the model’s applicability is experimentally demonstrated using a single-wheel test bed, which was constructed at the Space Robotics Laboratory to study the mechanics of rigid wheels interacting with rigid and deformable terrain, and to aid development of next-generation estimation, motion planning and control algorithms for planetary exploration rovers. Second, the model serves as a basis for developing an analytical relation of the longitudinal slip as a function of the slip angle. One limitation of this approach is that it requires prior knowledge of wheel–terrain parameters. Online methods of identification while the rover is traveling may be thought of and implemented. However, this problem is not addressed in this work.

In the robotics community, extensive research has been devoted to the study of visual motion estimation. It is possible to refer generally to two broad categories:

landmark-based and optic flow-based methods. The former methods recognize either natural or artificial landmarks in the environment and, then, infer the position of the robot, usually, by triangulation [13]. The latter approaches estimate the differential of successive images extracting optical flow vectors, which allow changes in the robot pose to be evaluated. Notable examples of this category include visual odometry methods, which were developed and demonstrated for rough-terrain robots [14, 15] and planetary rovers [1]. The purpose of visual odometry is that of incrementally estimating the motion of a mobile robot, by detecting and tracking interesting point-features of the environment over subsequent images, generally within a statistical framework for estimation. To this aim different interest operators were adopted such as Harris, Förstner, SIFT and Shi–Thomasi detector. In some cases, the search for good features to track may be simplified using motion information from other sensors [16] or selecting features on specific parts of the scene. Interestingly, point-features extracted from wheel tracks were used by the Mars exploration rover Opportunity for successful visual odometry on piles of sand at Meridiani Planum (see Section 5.1 in Ref. [1]). In this regard, the FTrace system represents a different approach. The similarities and differences with respect to existing literature can be summarized in the following points:

- It does not use optical flow or estimate incremental motion.
- It estimates the actual travel direction of the robot, i.e., the slip angle.
- It performs landmark tracking; however, the FTrace system does not use natural or artificial landmarks in a conventional sense, but it looks at the traces of the vehicle, which can be considered as special landmarks, generated by the vehicle itself.
- Trace tracking is performed using a Hough transform detector within a fuzzy inference model.

The onboard ability of estimating the lateral slip would be useful for many reasons, e.g., to adopt proper actions to revise the robot motion plan and avoid hazardous highly deformable terrains, or to modulate wheel torque to improve traction and limit slippage. In this paper, the slip angle measurement is used to improve pose estimation accuracy, in conjunction with traditional wheel encoders.

The paper is organized as follows. The salient theoretical aspects of the FTrace module are recalled in Section 2. Section 3 presents the combined-slip model along with its experimental validation and description of the sComp odometry. In Section 4, the FTrace system is proved to be effective and robust in field tests performed with the rover El-Dorado, and the sComp module is applied to correct encoder readings from slipping wheels. Finally, Section 5 concludes this paper.

2. FTrace System

The presence of shadows, occlusions and terrain unevenness can turn trace tracking into a very complex problem. A robust and efficient trace detection system must be able to filter out all disturbances and extract the marking of interest from a non-uniform background. In Fig. 2, a sample image set demonstrates the variety of terrain and environmental conditions that can be encountered. Figure 2a shows a scene where trace detection can be considered relatively easy thanks to the clearly defined imprint and uniform terrain texture. In Fig. 2b, extraction of the wheel trace is more difficult due to non-uniform terrain texture, whereas in Fig. 2c a more complex wheel trace is shown due to the presence of heavy shadowing. Finally, Fig. 2d refers to a condition where two imprints are present in the same scene. In this section, the theoretical basis of the method is briefly described, also providing experimental evidence of its effectiveness. For more details, we refer the reader to Ref. [12], rather than repeating this material here. One of the main advantages of using fuzzy inference systems is their flexibility. Although in our implementation, the FTrace system was optimized for the specific trace produced by El-Dorado's wheel, it may be easily adapted to other wheel traces with different geometrical characteristics.

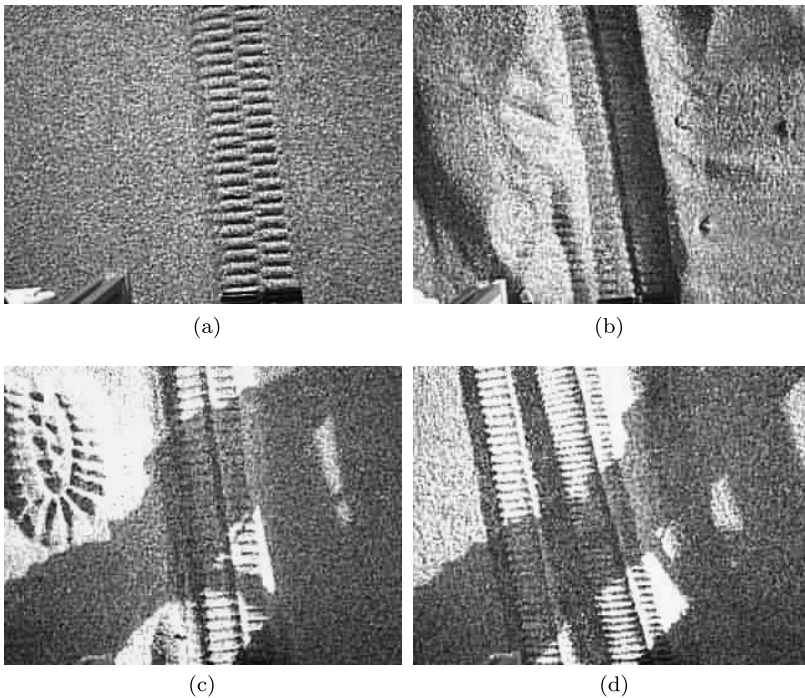


Figure 2. Sample images of terrain and wheel trace conditions: (a) uniform sandy terrain, (b) non-uniform terrain texture, (c) non-uniform terrain texture with noise due to shadowing and (d) different imprints present in the scene.

2.1. *Theoretical Model*

Let us refer to a simple schematic of the vehicle, known as the bicycle model [17], as shown in Fig. 3. The bicycle model neglects weight transfers, and assumes equal tires and slip angles on the wheels of the same axle. Under the assumption that the portion of the trace in the camera image, and the amount of sideslip between two consecutive images, is relatively small, it is possible to refer to a straight-line model of the wheel track, corresponding to its centerline. Then, the trace pose can be defined by the distance d_t with respect to the center of mass of the vehicle G , and the angle θ_t between the velocity vector of the rear wheel V_r and the wheel longitudinal axis. This angle is also usually referred to as the slip angle of the rear wheel α_r . With reference to Fig. 3, we can formally define the slip angle β of the whole vehicle as the angle between the velocity vector V of its center of mass G and the longitudinal axis X_v . Under the assumption of small angles, the following linearized relations hold between the slip angles and the velocity components:

$$\beta = \frac{V_y}{V_x} \tag{1}$$

$$\alpha_r - \delta_r = \frac{V_y - r \cdot b}{V_x} = \beta - \frac{b}{R_t}, \tag{2}$$

where V_x, V_y are the longitudinal and lateral component of the velocity vector V in the vehicle reference frame, δ_r is the rear steer angle, r is the rate of turn expressed in rad/s, R_t , defined as $R_t = V_x/r$, represents the distance of the instantaneous center of rotation from the longitudinal axis of the vehicle, and b is the distance between the rear axis and the center of mass G .

From (2), it is possible to estimate the slip angle β , given α_r from the FTrace system, δ_r and V_x from the steer and wheel encoders, and r by differentiation from

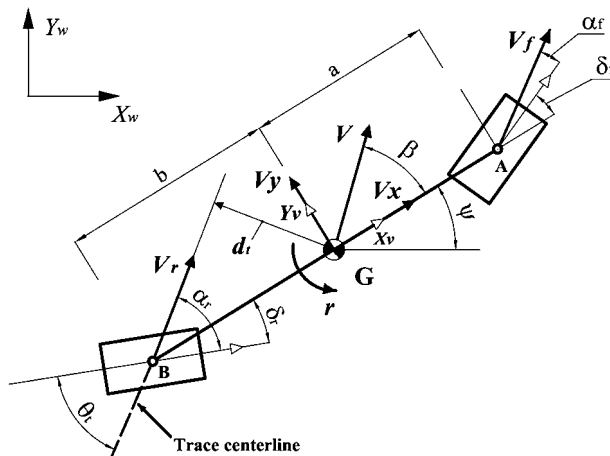


Figure 3. Model of the trace of the rear wheel with reference to a bicycle schematization of the robot.

the onboard compass. Note, however, that the contribution of the term b/R_t is typically very small and practically β can be confused with α_r , when also δ_r is null. Although (1) and (2) apply for a general maneuver with a given steer angle, in this paper we demonstrate the proposed system for the case of a straight path.

2.2. Trace Tracking

The FTrace module performs two main tasks:

- Extraction of trace candidates from the camera-acquired image and estimation of their pose with respect to the sensor, i.e., the vehicle, reference frame.
- Selection of the candidate that best fits to the trace model.

In order to determine which line best fits to the trace model, the system employs a robust Hough transform enhanced by fuzzy reasoning. The general approach is based on comparing the geometrical properties of each candidate with those of the trace model (as defined in Section 2.1) in both the image plane of the camera and the real-world, and defining deterministic conditions for model matching. The output of the FTrace is a fuzzy quantity that expresses the certainty that the line agrees exactly with the trace model. As a representative result, Fig. 4 shows a sample

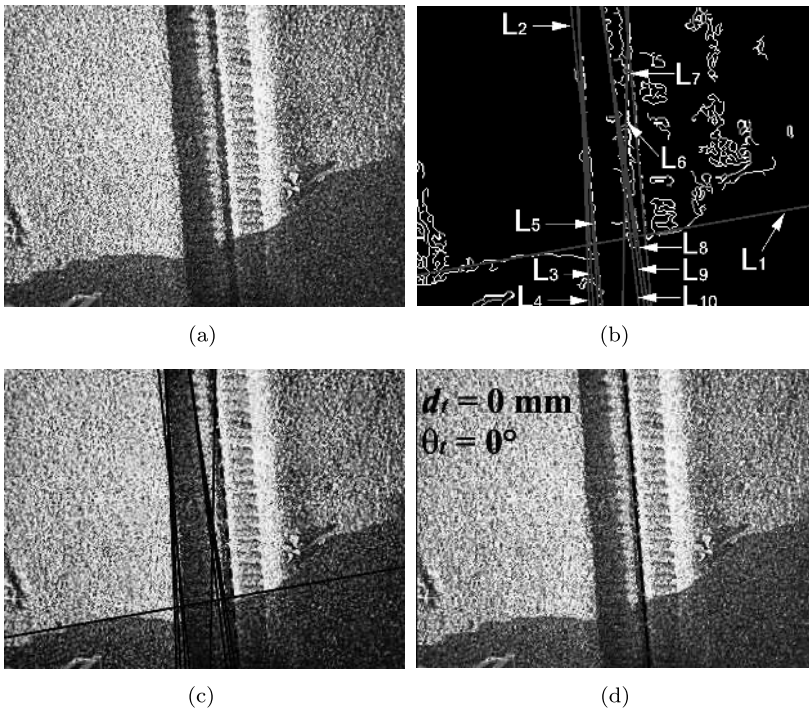


Figure 4. Application of the FTrace system to a sample image: (a) original scene, (b) and (c) application of edge detection and Hough transform to extract trace candidates, (d) output of the FTrace system. Note that no sideslip was detected in this image, i.e., $\theta_t = 0$.

image referring to a field trial of El-Dorado on sandy terrain. The FTrace system was able to extract 10 candidates from the original scene (Fig. 4a), as shown in Fig. 4b and 4c. The trace selection stage provided the confidence matches collected in Table 1. The lane marker, denoted L_7 in Fig. 4b and shown by a dotted line in Fig. 4c, yielded the greatest confidence level (92.3%) and was, therefore, selected as the best match. In Fig. 4d, the output of the FTrace system is overlaid over the original image along with the estimated values of d_t and θ_t .

3. Integrated Longitudinal and Lateral Slip

A proper wheel friction model is essential to develop an accurate position estimation system, since a ground vehicle’s motion is primarily determined by the friction forces transferred to terrain, *via* wheels. In general, a wheel is operated under the condition of both longitudinal and lateral slip. With reference to the single wheel of Fig. 5, a longitudinal slip ratio s_x and a slip angle β^w can be generally defined as:

$$s_x = 1 - \frac{V_x^w}{r^w \cdot \omega^w} \tag{3}$$

$$\beta^w = \arctan\left(\frac{V_y^w}{V_x^w}\right), \tag{4}$$

Table 1.

Degree of confidence in model matching of the trace candidates, extracted by the FTrace system from scene Fig. 4a

| | Candidate line | | | | | | | | | |
|----------------------|----------------|-------|-------|-------|-------|-------|-------|-------|-------|----------|
| | L_1 | L_2 | L_3 | L_4 | L_5 | L_6 | L_7 | L_8 | L_9 | L_{10} |
| Confidence match (%) | 2.1 | 3.1 | 3.0 | 2.4 | 2.6 | 20.1 | 92.3 | 30.3 | 26.7 | 24.2 |

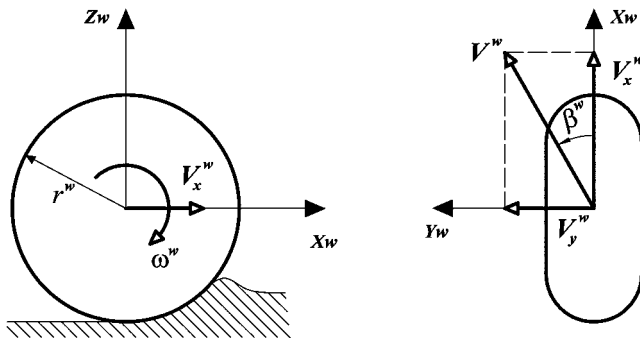


Figure 5. Longitudinal and lateral slip for a single wheel.

where V_x^w and V_y^w are the longitudinal and lateral components of the velocity vector V^w , r^w is the radius, and ω^w the angular velocity of the wheel. From a theoretical point of view, different wheel–terrain friction models can be used: analytical and empirical. Analytical models are based on terramechanics, which is that branch of mechanics that deals with the mechanisms underlying the interaction between a wheel (generally considered as rigid) and deformable, loose soil. Well-accepted physical models have been proposed in literature to relate the longitudinal and lateral friction force with the normal and tangential stress region at the wheel–terrain interface, taking into account some intrinsic terrain parameters such as cohesion and friction angle [7, 18, 19]. However, those models are highly nonlinear, over-parameterized and difficult to implement online [20]. The (semi)empirical models are based on curve-fitting techniques and easy to compute, overcoming the drawbacks of the analytical counterparts, while preserving good accuracy. In this paper, an empirically derived model for wheel–soil friction modeling is proposed, providing analytical relations for the longitudinal and lateral forces as a function of the slip ratio and the slip angle. It, thus, accounts for the coupling between the side and longitudinal force, known as the friction ellipse, as discussed later.

First, the model is presented, then its validity is demonstrated using a laboratory single-wheel test bed. Finally, a relation between longitudinal and lateral slip is derived for odometry correction.

3.1. Wheel–Soil Model

The model discussed in this section is based on the observation that the pure slip curves remain approximately similar in shape when the wheel runs at conditions that are different from the reference condition. The reference condition is defined here as the state where the wheel runs at either free rolling ($s_x = 0$) or at side slip equal to zero ($\beta^w = 0$). The functions representing the reference curves, which are found at pure slip conditions, are denoted with subscript ‘0’, and were found to be well experimentally defined as

$$F_{x,0}(s_x) = W \cdot (\mu \cdot (1 - e^{-\frac{C_x}{\mu \cdot W} \cdot s_x}) - A_x \cdot s_x) \quad (5)$$

$$F_{y,0}(\tan \beta) = W \cdot (\mu \cdot (1 - e^{-\frac{C_y}{\mu \cdot W} \cdot \tan \beta^w}) - A_y \cdot \tan \beta^w), \quad (6)$$

where $F_{x,0}$ and $F_{y,0}$ are the reference longitudinal and lateral force exchanged between the wheel and the soil (e.g., $F_{y,0}$ represents the side force *versus* slip angle relationship with longitudinal slip equal to zero), W is the vertical load acting on the wheel, and μ is the maximum coefficient of soil adhesion, C_x and C_y can be viewed as the longitudinal and lateral stiffness, respectively. The latter parameters are responsible for the slope of the traction curves in the low slip region, whereas A_x and A_y represent the slope in the high slip range, assuming positive or negative values depending on terrain. As we are dealing with, in general, a non-isotropic

wheel model, pure longitudinal and lateral slip characteristics are modeled as not identical. To address the problem of combined slip, the total slip can be introduced:

$$\sigma = \sqrt{s_x^2 + (\tan \beta^w)^2}, \tag{7}$$

and the longitudinal and lateral components of the total friction force can be defined:

$$F_x = \frac{\sigma_x}{\sigma} \cdot F_{x,0}(\sigma) \tag{8}$$

$$F_y = \frac{\sigma_y}{\sigma} \cdot F_{y,0}(\sigma). \tag{9}$$

According to this model, F_x increases with the slip ratio until it reaches a saturation value that can be approximated by:

$$F_{x,max}(\beta^w) = \lim_{s_x \rightarrow 1} F_x = \frac{\mu \cdot W}{\sqrt{1 + (\tan \beta^w)^2}}, \tag{10}$$

when considering that A_x is generally very small. The proposed model offers some advantages over other alternative experimental models: it retains some structures of the physics-based approaches, allows for independent values of wheel–soil stiffness in the lateral and longitudinal directions, the lateral and longitudinal forces are directly related to the soil adhesion in more transparent equations, and it is defined by few parameters, and thus easy to analyze.

3.2. Experimental Validation

A set of experiments was performed using the single-wheel test bed shown in Fig. 6. It is primarily composed of a wheel assembly, a carriage assembly, a control/acquisition system and a soil bin. The wheel assembly consists of a driven wheel mounted on an undriven vertical axis. Horizontal movement and steer angle of the wheel are actively controlled to allow different values of longitudinal slip ratio and slip angle to be investigated. A six-axis load sensor provides measurement of longitudinal and lateral forces developed in the wheel–soil interaction. The test

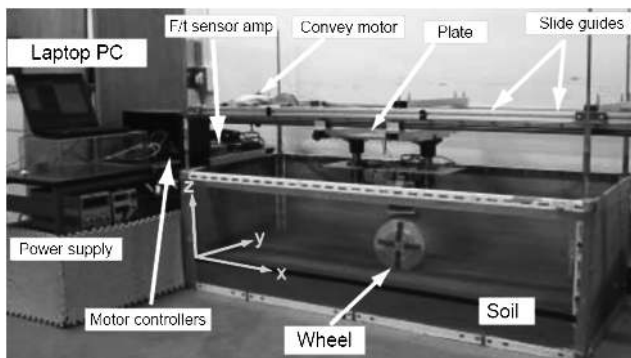


Figure 6. Wheel–terrain interaction test bed.

Table 2.
Soil parameters

| Soil | Cohesion c (kPa) | Internal friction angle φ ($^\circ$) | Density (kg/m^3) |
|-----------------------------|-----------------------|---|--------------------------------|
| Lunar soil simulant [22] | 0.8 | 30 | 1.6×10^3 |
| Loose sandy terrain [18] | 0.2–1.0 | 26–32 | $1.3\text{--}1.7 \times 10^3$ |

bed is designed for 5 to 25-cm diameter wheels, vertical loads in the 50–200 N range, wheel torques ranging from 0.1 to 5.0 Nm, linear velocities up to 10 cm/s, and drawbar pull forces up to 100 N. These ranges were chosen to be similar to those of current and future planned rover systems. More details of the single components of the system can be found in Ref. [21]. The so-called FJS-1 simulant was used [22], which reproduces real lunar soil. It was chosen as the test soil in our experiments since it is a well experimentally defined soil and available in the laboratory, and its properties fall in the average range of loose, sandy terrains, as shown in Table 2. Therefore, the behavior of a rigid wheel can be reasonably expected to be similar on both types of soil. A 92-mm radius, 110-mm wide rigid wheel with 10-mm high grousers was analyzed under a vertical load of $W = 6.6$ kg, slip ratio range of 0–0.8 and slip angle of 5–25°. Multiple experiments were conducted to guarantee repeatability, and experimental data are reported in terms of average measurement and standard deviation. In Fig. 7, the measured longitudinal force F_x is plotted as a function of slip ratio for increasing values of slip angle and the experimental data are compared with the predicted values obtained by the model. Similarly, Fig. 8 shows a comparison between the estimated lateral force F_y and the empirical model for increasing values of slip angle. In both Figs 7 and 8, the agreement between the experimental data and the model is good, attesting to the feasibility of this approach. The predicted F_x always lies within the level of confidence of the measurements. The lateral force F_y is also well modeled for small and medium slip angles ($\beta^w = 5\text{--}10^\circ$), whereas it appears slightly overestimated for high slip angles.

3.2.1. Model Tuning

In order to compare the experimental results with the model, the wheel–soil parameters associated with the model need to be tuned. Based on the physical understanding of the model, the following procedure was developed as part of this research, which led to the results summarized in Table 3:

- (i) From (10), it is possible to adjust μ to obtain the correct $F_{x,\max}$ for small slip angles (i.e., $F_{x,\max} \simeq \mu \cdot W$).

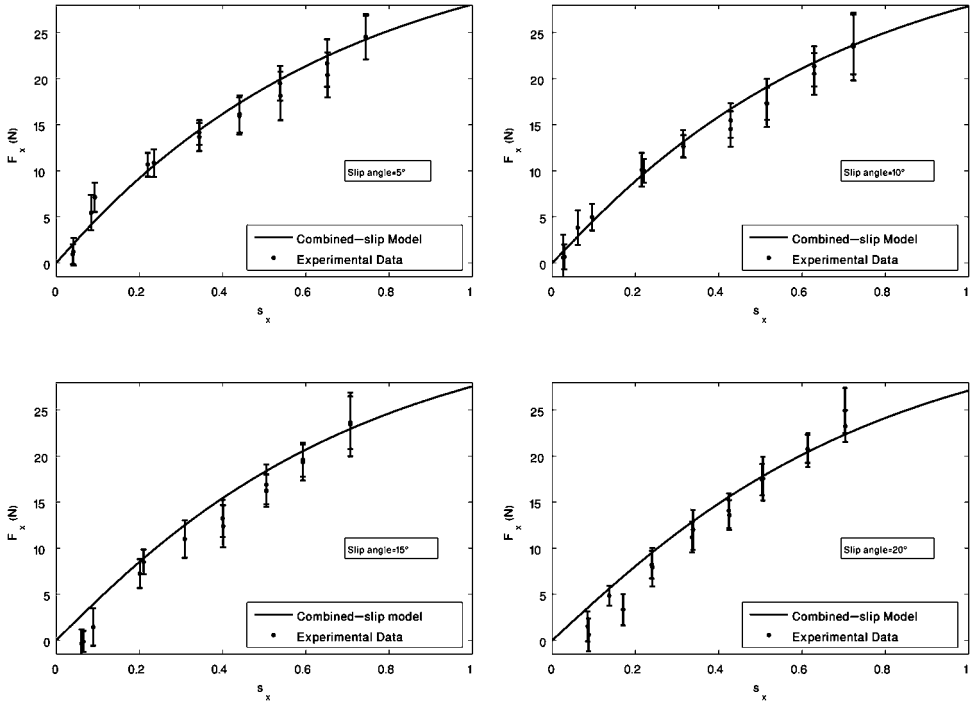


Figure 7. Longitudinal force *versus* slip ratio. Black dots with error bar: experimentally determined data with indication of statistical spread. Black solid line: combined-slip model.

- (ii) From (9), the value of C_y can be determined by matching F_y for small values of slip ratio.
- (iii) From (8), it is possible to tune C_x so that F_x agrees with the experimental data for small slip ratio.
- (iv) Finally A_x and A_y can be determined from (8) and (9), respectively, by fitting F_x and F_y at high slip ratio.

Note that the value of C_y is larger than C_x . This can be explained when considering the so-called ‘bulldozing’ resistance, acting on the side wall of the wheel [7].

3.3. Relating Longitudinal and Lateral Slip

In general, the presence of a lateral force, and thus of a slip angle, decreases the availability of adhesion along the longitudinal direction. For a given longitudinal force, the wheels of the vehicle will build up a higher slip ratio if a lateral disturbance force is also present. This is shown in Fig. 9, where F_x predicted by the model is plotted as a function of s_x for different values of slip angle. Similarly, the tractive effort will reduce the cornering force that can be generated for a given slip angle as illustrated in Fig. 10, where the lateral force is plotted as a function of slip ratio s_x for various slip angles. If longitudinal force is plotted against lateral force

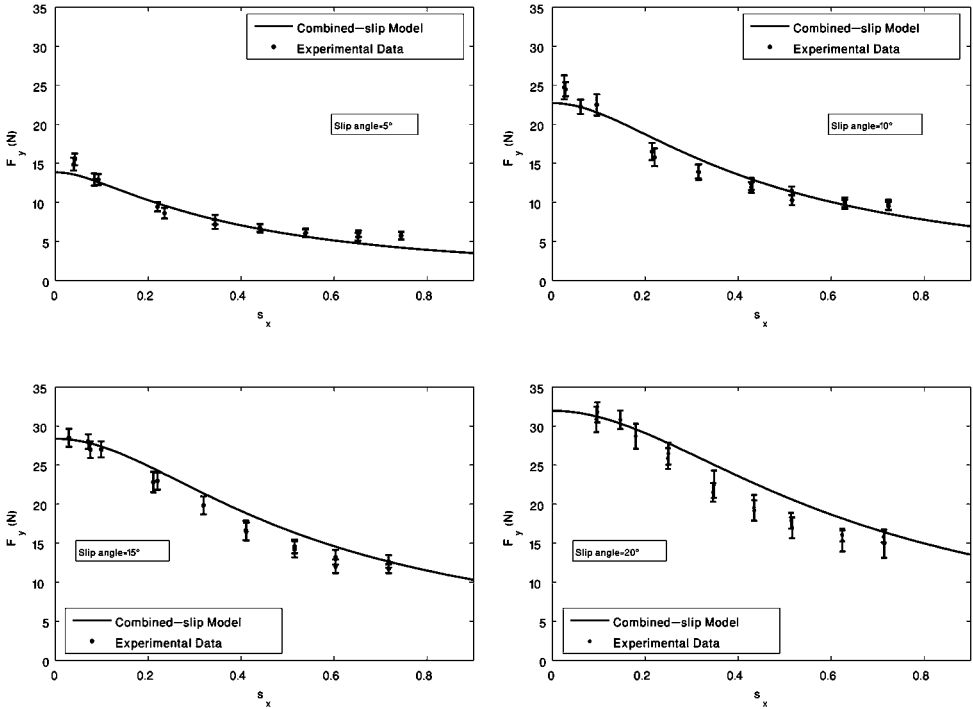


Figure 8. Lateral force *versus* slip ratio. Black dots with error bar: experimental determined data with indication of statistical spread. Black solid line: combined-slip model.

for various slip angles, these curves can be well approximated by friction ellipses, with major axes dependent on the slip angle:

$$\left(\frac{F_x}{F_{x,\max}(\beta^w)}\right)^2 + \left(\frac{F_y}{F_{y,\max}(\beta^w)}\right)^2 = 1. \tag{11}$$

$F_{y,\max}(\beta^w)$ is computed by setting the slip ratio $s_x = 0$ in (9), whereas $F_{x,\max}(\beta^w)$ is given by (10). This is shown in Fig. 11, where it can be seen that for a given slip angle, the lateral force decreases gradually with the increase of the tractive effort and *vice versa*. When a wheel is operated under conditions of simultaneous longitudinal and lateral slip, the respective forces depart markedly from those values derived under independent conditions. The application of longitudinal slip generally tends to reduce the lateral force at a given slip angle and, conversely, the application of slip angle reduces the longitudinal force that develops under a given traction condition.

One should note that for low-speed planetary rovers, the centrifugal force acting on the rover during steering maneuvers is very small and it does not affect significantly the lateral dynamics of the vehicle. Thus, the only practical case of interest for combined longitudinal and lateral slip corresponds to the presence of

Table 3.

Wheel–soil parameters of the model obtained by experimental data fitting for lunar soil simulant

| μ | $C_x(N)$ | $C_y(N)$ | A_x | A_y |
|-------|----------|----------|-------|-------|
| 0.6 | 55 | 200 | 0.02 | 0.04 |

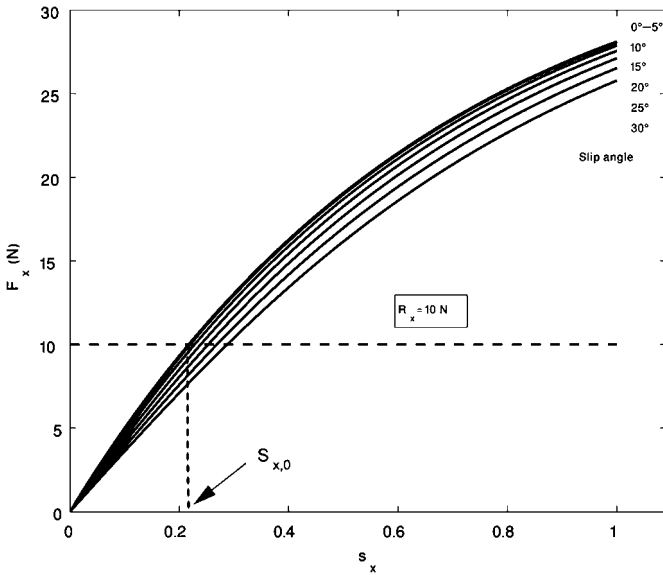


Figure 9. Longitudinal force as function of the slip ratio for different values of the slip angle. The tractive effort for a slope with inclination of $\theta = 12^\circ$ is also shown by a dashed line.

a transversal inclination of the terrain (bank angle), when the lateral component of the vehicle’s weight force acts as an external disturbance.

Let us consider a scenario with the robot driving up a slope at constant speed. The longitudinal tractive effort for one wheel of the robot is approximately equal to $R_x = W \cdot \sin\theta$, where θ is the inclination of the slope and W is one-quarter of the total vehicle weight. Note that this value does not change if a simultaneous transversal inclination is also present. The correspondent longitudinal slip can be obtained from the graph of Fig. 9 by intersecting the value of the given R_x with the curve of F_x for $\beta^w = 0$. This value, denoted as $s_{x,0}$, can be regarded as the reference value of the slip ratio in the absence of lateral drift for the given slope. If a lateral force is also present, due to a contemporary lateral inclination of the terrain, the wheel will travel with an associated slip angle, resulting in a decrease in the adhesion availability along the longitudinal direction. Thus, in order to balance the same tractive effort, the wheel will need to build up a larger slip ratio s_x . The relationship between the slip ratio and the slip angle can be numerically obtained

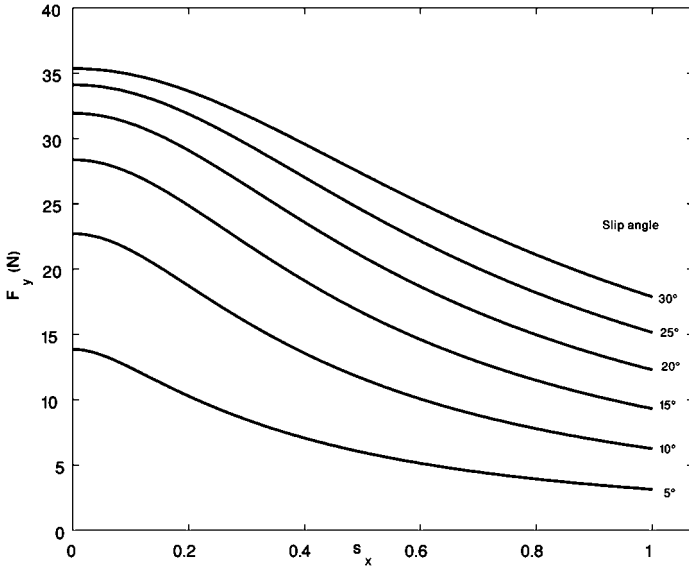


Figure 10. Lateral force as function of the slip ratio for different values of the slip angle.

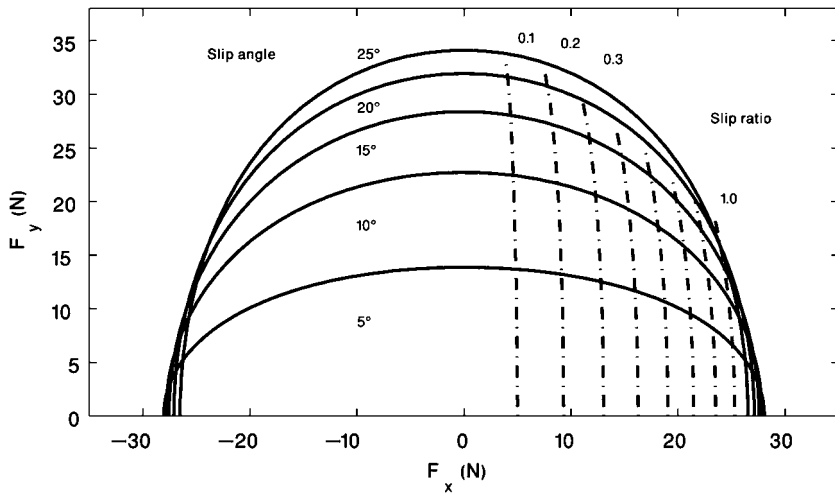


Figure 11. Friction ellipsis relating the longitudinal and lateral force for constant slip angles. Note that the curves at constant slip ratio are shown by a dash-dotted line.

under the assumption of constant tractive effort R_x and extended to the behavior of the entire vehicle. The result is shown in Fig. 12. The curve can be approximated by a linear equation without losing much accuracy:

$$s_x = \begin{cases} s_{x,0}, & \beta \leq \beta_0 \\ s_{x,0} + k \cdot (\beta - \beta_0), & \beta > \beta_0, \end{cases} \quad (12)$$

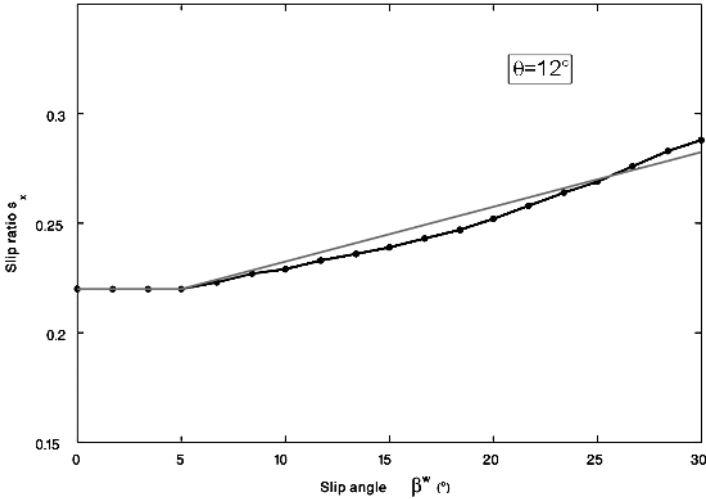


Figure 12. Slip ratio *versus* slip angle relationship for a given terrain slope ($\theta = 12^\circ$). Black line with dots: simulated slip model; gray solid line: linear approximation.

where k is the slope of the linear approximation and β_0 marks the beginning of the increase in slip ratio due to lateral slip. The simplified model has the advantage of being entirely defined by two constants, k and $s_{x,0}$; it is easy to implement in software and has low computational time. We recognize that the level of approximation of the linear model depends on the value of the tractive effort R_x , i.e., the inclination of the slope. However, in the typical operational range of the robot $s_x = [0, 0.6]$ and for the usual slopes traversed ($\theta = [5, 20]^\circ$), (12) represents a good estimate. Note that out of this range, the behavior of the robot may become unstable with large drift and (12) would lose its validity. Higher-order models may also be applied instead of (12) with small improvement in accuracy at the cost of a greater complexity. We also recognize that the values of the model's parameters depend on the tractive effort and the type of soil. For a given terrain, both k and $s_{x,0}$ increase with the inclination of the slope. Thus, by measuring the current pitch angle of the robot with an onboard sensor, it would be possible to adopt on-line methods of identification, changing adaptively their values.

4. Experimental Results

In this section experimental results are presented, aimed at validating our approach for lateral slip estimation by visual observation of the wheel trace. The correction method for wheel slippage-incurred odometry errors, based on the longitudinal slip *versus* lateral slip function $s_x(\beta)$, defined in Section 3.3, is also experimentally demonstrated. The FTrace system was tested in the field using the rover El-Dorado, outfitted with a cost-effective webcam acquiring at 5 Hz and with a field of view on the ground plane corresponding to a 60-cm long \times 80-cm wide area behind

the left rear wheel. The test field was located on the shoreline of a sandy beach, comprising large flat areas and sparse mounds of different extensions and heights. In all experiments, the rover was remotely controlled using a wireless joypad and commanded to follow a straight-line path with a travel speed of about 8 cm/s. Two types of environment were considered:

- *Set A*: sandy relatively flat terrain. These experiments were aimed at evaluating undue errors of the FTrace system incurred by low-slippage terrain.
- *Set B*: sandy non-flat terrain, including driving uphill or sideways on sandy slopes with substantial lateral slip.

The entire experimental area was within the distance range (order of tens of meters) of a laser-based absolute positioning system that provided the ground-truth translational position (x, y, z) with respect to a global coordinate frame. The ground-truth sideslip angle of the robot β_g was estimated as the difference between the absolute vehicle heading direction ψ_1 , derived by the laser position-measurement system, and the vehicle heading ψ , measured by the onboard compass

$$\psi_1 = \arctan\left(\frac{\dot{y}}{\dot{x}}\right) \quad (13)$$

$$\beta_g = \psi_1 - \psi. \quad (14)$$

In the remainder of this section, the performance of the FTrace system are first discussed in terms of robustness and accuracy, and then the results obtained from the sComp odometry are presented.

4.1. FTrace System: Robustness Analysis

The FTrace system was tested over a total of 15 016 images (about 250 m of overall travel distance) with Table 4 showing the results collected in both sets of experiments. Figure 13 also shows some typical results obtained from sample images of different tests. The percentage of false positives, i.e., a trace marker detected when actually there is no trace marker, was less than 0.3% and limited to the initial moments of robot's motion when no wheel track was present on the ground yet. Note that in the initial stage, the FTrace system relies only on Hough transform to extract strong lines from the scene, which pass through the wheel center, whereas the fuzzy inference system kicks in after the rover begins traveling. Conversely, false negatives arise when the trace marker is present in the image, but the system is not able to detect it at all and does not return any information. The percentage of false negatives was less than 3%, and due largely to poor image segmentation and camera calibration errors (80%), and model approximation (20%). In those cases the last detected wheel trace is retained for comparison with the successive scenes. This approach proved successfully since the number of consecutive false negatives was always less than 3 (below 0.6 s). Finally, misidentifications refer to cases in which a trace marker is present in the image, but the system fails in recognizing

Table 4.

Results obtained from the FTrace system for different terrains (set A: flat sandy terrain; set B: non-flat terrain)

| Set | Frames | False positives (%) | False negatives (%) | Misidentifications (%) |
|-----|--------|---------------------|---------------------|------------------------|
| A | 2560 | 0.1 | 1.5 | 0.0 |
| B | 12 456 | 0.2 | 2.7 | 0.8 |

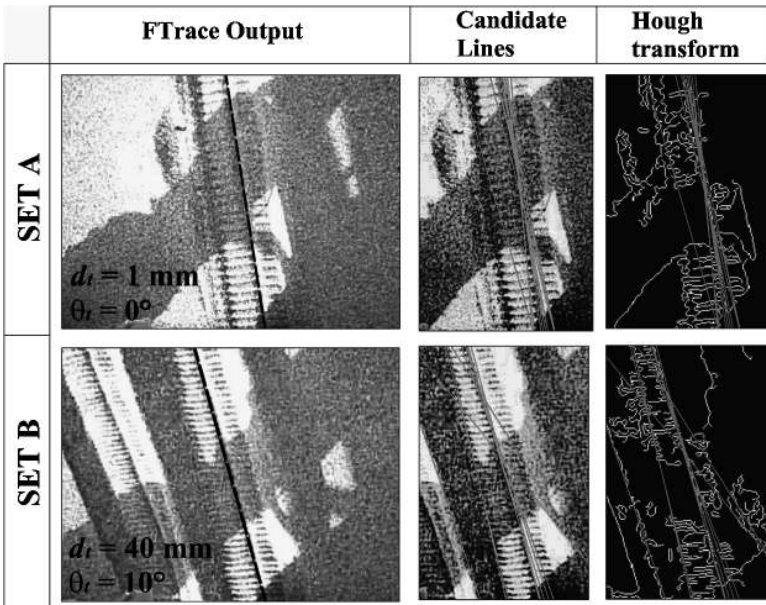


Figure 13. Results obtained from the FTrace system under various terrain and environmental conditions. See Table 4 for more details.

it properly and returns wrong information. In all tests, misidentifications were less than 1%. Overall, the system proved to be robust to disturbances due to heavy shadowing, non-uniform terrain texture and presence of overlapping imprints. Note that the knowledge of the pose of the trace in one image is used to determine the region of interest to be searched for model detection in the next frame. This makes the trace search more accurate and reduces computational requirement by eliminating much of the scene, as shown by the second and third column of Fig. 13. In the first column of Fig. 13, the detected trace and the output of the FTrace system is overlaid over the original image.

4.2. FTrace System: Accuracy Analysis

The accuracy of the FTrace system in estimating the lateral drift of the robot was assessed in two experiments on non-flat terrain. In the first test, El-Dorado was driven

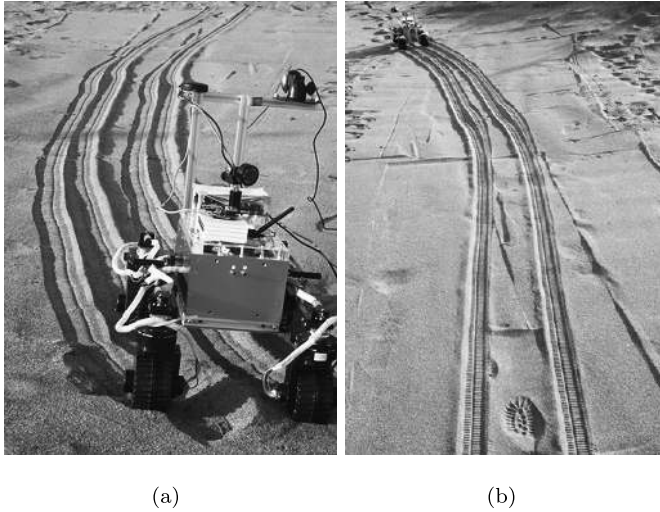


Figure 14. Traces produced by the wheels of the rover at the end of a sandy slope traverse: (a) front view and (b) rear view.

up an approximately 5° sandy slope. During its path, the robot climbed sideways on a large mound (Section 4.2.1), resulting in continuous and almost constant lateral drift. In the second experiment, El-Dorado was also commanded to climb up an approximately 5° sandy slope, but along its traverse it negotiated a series of consecutive small mounds (Section 4.2.2), experiencing alternating episodes of absence of drift, and combined longitudinal and lateral slip.

4.2.1. Sideways Climbing

Figure 14 shows the position of El-Dorado and the imprints produced by its wheels at the end of the run, from a front and rear view, respectively. The total travel distance resulted in about $D = 7$ m. The slip angle, derived from the FTrace system, is compared with the ground-truth data in Fig. 15. The two curves show good agreement with a root mean square (r.m.s.) error less than 1.5° . The FTrace system detected effectively the onset of sideslip and its successive trend throughout the experiment. Two different stages can be distinguished during the test. In the first stage, referring to the first 60 s, the robot followed its intended straight path without any significant drift. This is demonstrated by the two wheel traces parallel to the direction of motion. The second stage marks the onset of sideslip caused by the external lateral force acting on the rover due to the transverse inclination of the terrain. As a direct consequence, the angle of inclination of the wheel traces changes (see also Fig. 14b), attesting to the feasibility of our approach.

4.2.2. Negotiation of Sandy Mounds

The final position of the rover is shown in Fig. 16, resulting in a total travel distance of about $D = 13$ m. Figure 17 shows the slip angle as estimated by the FTrace system, compared with the ground truth data. Also in this second experiment, a good

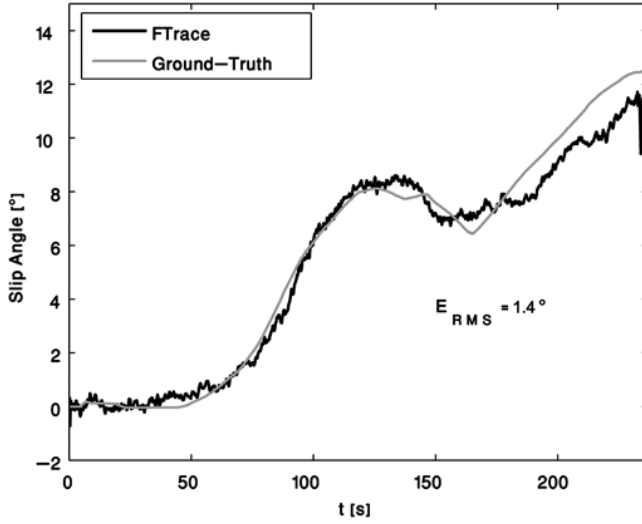


Figure 15. Accuracy of the FTrace system in estimating slip angle for a sandy slope traverse.

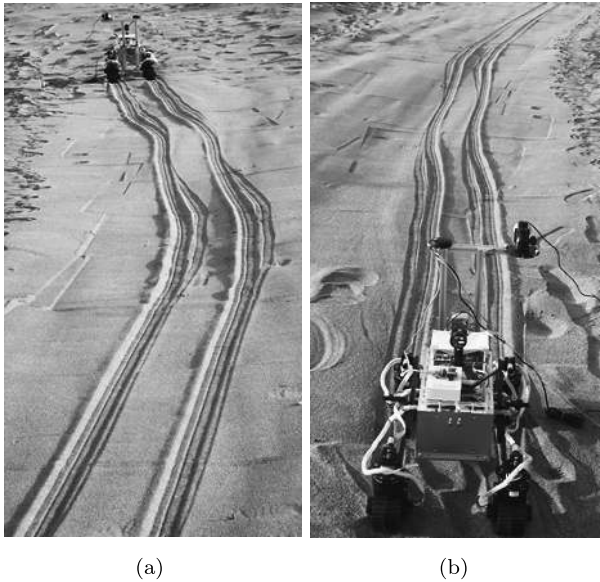


Figure 16. Tracks produced by the wheels of the rover after the negotiation of consecutive sandy mounds: (a) front view and (b) rear view.

match between the two curves can be observed with a r.m.s. error less than 2° . Both the two large drifts experienced by the robot were successfully detected and measured.

In all similar experiments, the accuracy of the FTrace system was consistent with the results presented above, which can, then, be regarded as of general significance.

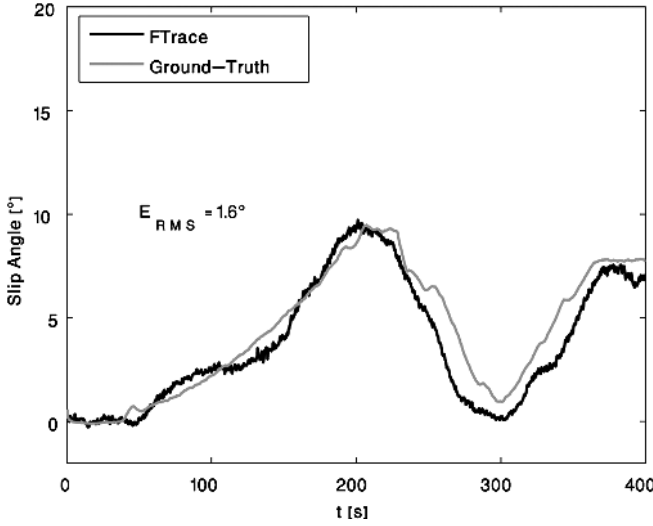


Figure 17. Effectiveness of the FTrace system in estimating the slip angle during negotiation of sandy mounds.

Finally, one should note that at the typical low speeds of planetary rovers the FTrace system provides a fast measurement update every few centimeters of travel distance (less than 2 cm in our case), allowing the system accuracy not to be significantly affected by the straight-line approximation of the wheel track model.

4.3. Slippage Correction (*sComp*)

In this section, we discuss the effectiveness of the *sComp* method by applying the proposed correction of slippage-incurred odometry errors to the experiments presented in Section 4.2. With reference to Fig. 3, the slip-corrected velocity components of the robot in a body-fixed reference system can be obtained as:

$$V_x = \begin{cases} r^w \cdot \omega \cdot (1 - s_{x,0}), & \beta \leq \beta_0 \\ r^w \cdot \omega \cdot (1 - s_{x,0} + k \cdot (\beta - \beta_0)), & \beta > \beta_0 \end{cases} \quad (15)$$

$$V_y = V_x \cdot \tan \beta, \quad (16)$$

where the slip angle β is measured by the FTrace system and ω is the angular speed of wheels measured by encoders. Note that, due to the high gear ratio (1500:1) of El-Dorado’s drive motors, the angular speed of the wheels does not change significantly even in the presence of high combined slip and, thus, ω can be estimated by averaging between the four wheels. In order to know the motion of the vehicle in a fixed reference frame, the following transformation is required,

$$\begin{bmatrix} \bar{V}_x \\ \bar{V}_y \end{bmatrix} = \begin{bmatrix} \cos \psi & -\sin \psi \\ \sin \psi & \cos \psi \end{bmatrix} \cdot \begin{bmatrix} V_x \\ V_y \end{bmatrix}, \quad (17)$$

where \bar{V}_x and \bar{V}_y are the velocity components in the fixed reference frame and ψ is the absolute orientation of the robot in the inertial frame that can be measured by

the onboard compass. Finally, the path of the robot can be obtained from (17) by integration.

4.3.1. Sideways Climbing

We recall from Section 3.3 that $s_x(\beta)$ is a linearized function defined by the parameters $s_{x,0}$ and k . These parameters were experimentally found for the given terrain through a minimization process using the absolute ground-truth measurements provided by the laser-based position estimation system. In Fig. 18, the performance of the system in terms of estimation of longitudinal slip s_x is compared with the ground-truth data. The curves show good agreement; the r.m.s. error in the measurement of the slip ratio was less than 0.1. Figure 19 shows the path followed by the robot as estimated by plain odometry by a dashed black line. The path derived from our slippage-compensated odometry is shown by a solid gray line. Both data can be compared with the ground-truth shown by a solid black line. An absolute error E was computed for the estimation of the final position of the robot $P = (P_x, P_y)$ as:

$$E = \sqrt{(P_x - P_x^{\text{gt}})^2 + (P_y - P_y^{\text{gt}})^2}, \quad (18)$$

where the superscript ‘gt’ refers to ground-truth data. We refer to this type of error since we believe that it provides a better description of the performance of the system, by serving also as an indicator of the typical accumulation error of odometry. Plain odometry estimated an apparent straight path, without detecting any occurrence of slippage and the associated deviation of the vehicle from the intended course. The error in the estimation of the final position of the robot using odometry was $E_e = 2.84$ m. If odometry is enhanced by measuring the actual heading of the robot with an onboard compass rather than wheel encoders, the error was decreased to $E_{oc} = 2.50$ m. When using the sComp odometry the final position error

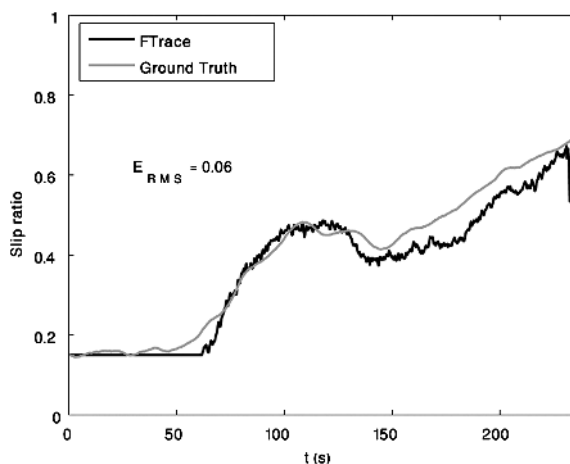


Figure 18. Slip ratio estimation during the traverse of a sandy slope.

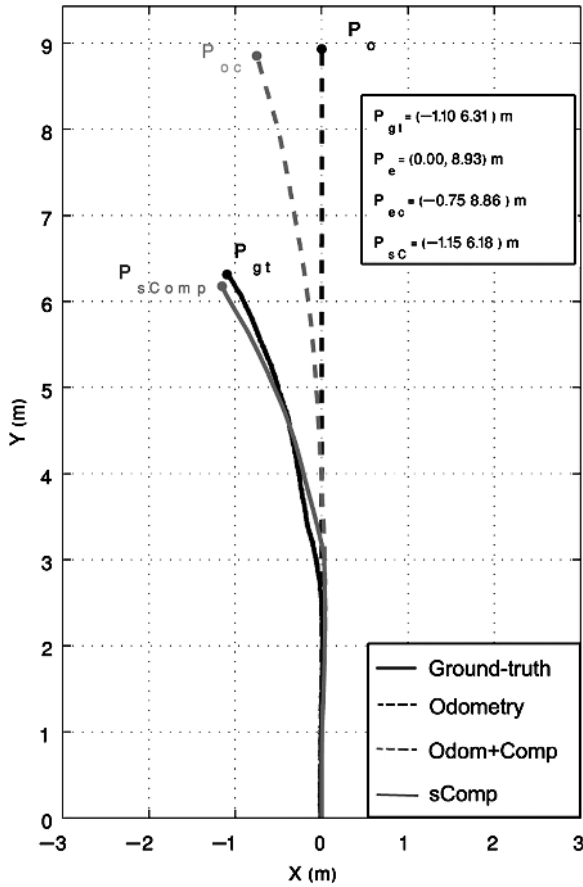


Figure 19. Position estimation of the rover path during the traverse of a sandy slope.

was limited to $E_{sC} = 0.14$ m with an overall reduction of 95% with respect to plain odometry and 83% compared to compass-enhanced odometry.

4.3.2. Negotiation of Sandy Mounds

In order to prove the validity of the integrated slip model, the set of parameters of the function $s_x(\beta)$ used in the previous experiment, denominated ‘sideways climbing’, was also adopted for this test. The longitudinal slip, inferred from the FTrace system, is compared with the ground-truth data in Fig. 20. A good match between the two curves was found with a r.m.s. error of 0.1. Figure 21 compares the path of the robot as estimated by plain odometry and using the sComp odometry. Again, plain odometry estimated a seeming straight path, shown by a black dashed line, without detecting any deviation of the vehicle from the desired course. The error in the estimation of the final position of the robot was $E_e = 2.90$ m, using plain odometry. If odometry is enhanced by the onboard compass (gray dashed line), the error was reduced to $E_{ec} = 1.98$ m. When using the sComp odometry the same error was

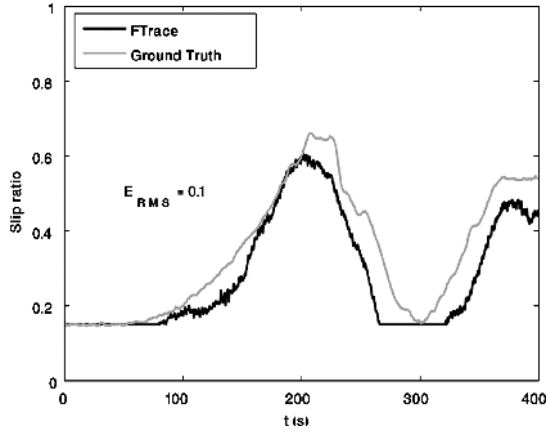


Figure 20. Slip ratio estimation during the negotiation of sandy mounds.

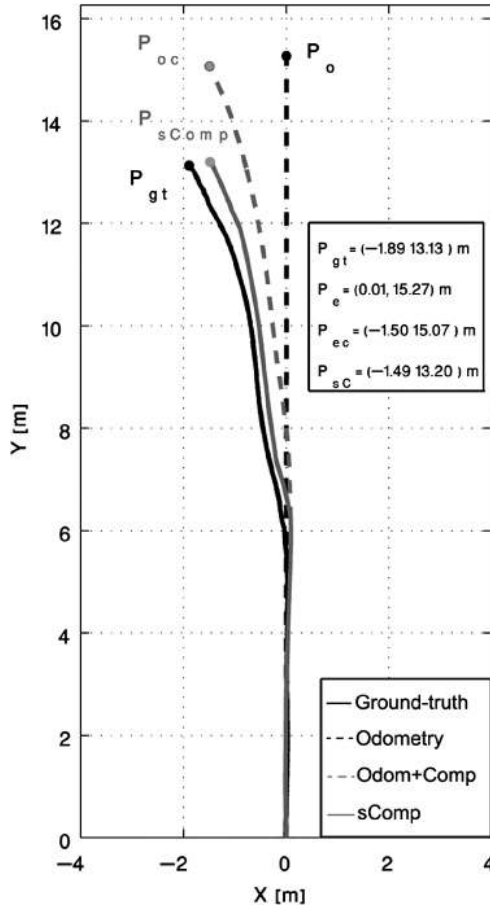


Figure 21. Position estimation of the rover during the negotiation of sandy mounds.

Table 5.

Experimental conditions and results for the two experiments described in Sections 4.2 and 4.3 (see Figs 19 and 21 for detailed results)

| Test | Terrain features | FTrace system | | Final position error (m) | | | Error reduction (%) |
|------|---|----------------------------|----------|--------------------------|-------------------|----------------|---------------------|
| | | E_{β} ($^{\circ}$) | E_{sx} | Plain odometry | Enhanced odometry | sComp odometry | |
| 1 | Moderate sandy slope with simultaneous transverse inclination | 1.4 | 0.06 | 2.84 | 2.50 | 0.14 | 95 |
| 2 | Moderate sandy slope with sparse mounds | 1.6 | 0.10 | 2.9 | 1.98 | 0.41 | 86 |

E_{β} is the r.m.s. error in the estimation of the slip angle; E_{sx} refers to the error in the slip ratio measurement.

limited to $E_{sC} = 0.41$ m with a reduction of 86% with respect to plain odometry, and 80% compared to compass-enhanced odometry.

An overview of the experimental results presented in this section is shown in Table 5.

5. Conclusions

In this paper, a novel method for sideslip estimation was presented, based on observing the wheel traces left by a robot during its traverse of loose sandy terrains. The paper also discussed an integrated longitudinal and lateral wheel–terrain slip model and its application to improve the position estimation accuracy of a mobile robot. Comprehensive experiments in the field demonstrated the overall effectiveness of the proposed approach. The FTrace method was able to measure the slip angle of the robot with a worst case of less than 3% of failed observations and 1.6° of accuracy. The sComp odometry was also shown to be effective in correcting odometry errors caused by wheel slippage during traverse of sandy slopes. Errors were reduced by up to 95% when compared with conventional dead-reckoning on the same terrain. Even under conditions of extensive and alternating slip, the system kept odometry errors to well under 4% of the total travel distance.

Acknowledgements

The authors would like to thank Dr Annalisa Milella for precious discussions on the visual algorithms. The authors are also thankful to the Japanese Society for the Promotion of Science for supporting the project through Fellowship P06061.

References

1. M. Maimone, Y. Cheng and L. Matthies, Two years of visual odometry on the Mars exploration rovers, *J. Field Robotics* **24**, 169–186 (2007).
2. T. Huntsberger, H. Aghazarian, Y. Cheng, E. T. Baumgartner, E. Tunstel, C. Leger, A. Trebi-Ollennu and P. S. Schenker, Rover autonomy for long range navigation and science data acquisition on planetary surfaces, in: *Proc. IEEE Int. Conf. on Robotics and Automation*, Washington, DC, vol. 3, pp. 3161–3168 (2002).
3. F. Gustafsson, Slip-based tire-road friction estimation, *Automatica* **33**, 1087–1099 (1997).
4. G. Reina, L. Ojeda, A. Milella and J. Borenstein, Wheel slippage and sinkage detection for planetary rovers, *IEEE/ASME Trans. Mechatron.* **11**, 185–195 (2006).
5. L. Ojeda, D. Cruz, G. Reina and J. Borenstein, Current-based slippage detection and odometry correction for mobile robots and planetary rovers, *IEEE Trans. Robotics* **22**, 366–378 (2006).
6. C. Ward and K. Iagnemma, Model-based wheel slip detection for outdoor mobile robots, in: *Proc. IEEE Int. Conf. on Robotics and Automation*, Rome, pp. 2724–2729 (2007).
7. G. Ishigami, A. Miwa, K. Nagatani and K. Yoshida, Terramechanics-based model for steering maneuver of planetary exploration rovers on loose soil, *J. Field Robotics* **24**, 233–250 (2007).
8. H. Tan and Y. Chin, Vehicle antilock braking and traction control: a theoretical study, *Int. J. Syst. Sci.* **23**, 351–365 (1992).
9. Bosch Group, *Automotive Handbook*, 5th edn. Robert Bosch, Plochingen (2000).
10. R. Anderson and D. Bevy, Estimation of slip angles using a model based estimator and GPS, in: *Proc. Am. Control Conf.*, Boston, MA, vol. 3, pp. 2122–2127 (2004).
11. J. Hahn, R. Rajamani and L. Alexander, GPS-based real-time identification of tire-road friction coefficient, *IEEE Trans. Control Syst. Technol.* **10**, 331–343 (2002).
12. G. Reina and K. Yoshida, Slip angle estimation for lunar and planetary robots, *Int. J. Intell. Control Syst. (Special Issue on Field Robotics)* **13**, 15–24 (2008).
13. G. DeSouza and A. Kak, Vision for mobile robot navigation: a survey, *IEEE Trans. Pattern Anal. Mach. Intell.* **24**, 237–267 (2002).
14. D. Nistér, O. Naroditsky and J. Bergen, Visual odometry, in: *Proc. IEEE Computer Society Conf. on Computer Vision and Pattern Recognition*, Washington, DC, pp. 652–659 (2004).
15. K. Konolige, M. Agrawal and J. Sola, Large-scale visual odometry for rough terrain, in: *Proc. Int. Symp. on Research in Robotics*, Hiroshima, pp. 1–6 (2007).
16. D. Helmick, S. I. Roumeliotis, Y. Cheng, D. S. Clouse, M. Bajracharya and L. Matthies, Slip compensated path following for planetary exploration rovers, *Adv. Robotics* **20**, 1257–1280 (2006).
17. G. Genta, *Motor Vehicle Dynamics*. World Scientific, Singapore (2003).
18. J. Wong, *Theory of Ground Vehicles*. Wiley-Interscience, New York (2001).
19. G. Bekker, *Introduction to Terrain-Vehicle Systems*. University of Michigan Press, Ann Arbor, MI (1969).
20. K. Iagnemma, and S. Dubowsky, *Mobile Robots in Rough Terrain: Estimation, Motion Planning, and Control with Application to Planetary Rovers (Springer Tracts in Advanced Robotics 12)*. Springer, Berlin (2004).
21. G. Ishigami, Terramechanics-based analysis and control for lunar/planetary exploration robots, *PhD Thesis*, Graduate School of Engineering, Tohoku University, Sendai (2008).
22. H. Kanamori, S. Udagawa, T. Yoshida, S. Matsumoto and K. Takagi, Properties of lunar soil simulants manufactured in Japan, in: *Proc. Int. Conf. and Exposition on Engineering, Construction, and Operations in Space*, Albuquerque, NM, pp. 462–468 (1998).

About the Authors



Giulio Reina received the Laurea degree and the Research Doctorate degree from the Politecnico of Bari, Italy, in 2000 and 2004, respectively, both in Mechanical Engineering. From 2002 to 2003, he worked at the University of Michigan Mobile Robotics Laboratory as a Visiting Scholar. In 2007, he was awarded a Japanese Society for Promotion of Science fellowship for a 1-year research at the Space Robotics Laboratory of the Tohoku University, Sendai, Japan. Currently, he is an Assistant Professor in Applied Mechanics with the Department of Engineering for Innovation, University of Salento, Lecce, Italy. His research interests include planetary rovers, mobility and localization on rough terrain, computer vision applied to robotics, and agricultural robotics.



Genya Ishigami received ME and PhD degrees from Tohoku University, Japan, in 2005 and 2008, respectively. He has been a Research Fellow of the Japan Society for the Promotion of Science, from 2006 to 2008. He has been a Postdoctoral Associate at the Massachusetts Institute of Technology, since 2008. His research interests are in the areas of mobility analysis including modeling robot–terrain interaction, design, planning and control for application to lunar/planetary exploration rovers, rescue robots and field robots.



Keiji Nagatani received the PhD degree from the University of Tsukuba in 1997. From 1997 to 1999, he was a Postdoctoral Researcher in the Mechanical Engineering Department, Carnegie Mellon University, USA. From 1999 to 2005, he was a Lecturer in the System Engineering Department, Okayama University, Japan. He is currently an Associate Professor in the Department of Aerospace Engineering, Tohoku University, since 2005. His research interest is in the area of mobile robotics that includes control, planning and map building for planetary rovers and tracked vehicles.



Kazuya Yoshida received BE and MS degrees in Mechanical Engineering science from Tokyo Institute of Technology, Japan, in 1984 and 1986, respectively. He received the DE degree from Tokyo Institute of Technology, in 1990. He served as a Research Associate of Tokyo Institute of Technology, from 1986 to 1994, and a visiting scientist of Massachusetts Institute of Technology, USA, in 1994. From 1985 to 2003, he was appointed as an Associate Professor of Tohoku University, Japan, and since 2003 as a Professor in Department of Aerospace Engineering, Tohoku University. He has also been serving as a Visiting Lecture of the International Space University, since 1998. His research activities include dynamics and control issues of various types of space robots, covering from free-flying robots to planetary exploration rovers. Recently, his activities have been extended to terrestrial applications of space technology, such as telerobotics for disaster mitigation missions.